

Ag-Embedded Carbon Nanotube Bucky Papers for Lithium Metal Full Batteries

Jun Su Kim, Chanmin Park, Dong Hyun Min, Taehun Kang, Jin Suk Byun, Suhyeon Kim, Won Il Kim, Hyun Gyu Cho, Hyun Chul Kim, Min Ju Kim, and Ho Seok Park*

Lithium (Li) metal anodes have received significant attention owing to their high theoretical capacity and low redox potential. Herein, a 3D bucky paper-based host is demonstrated, consisting of multi-walled carbon nanotubes (MWCNT) and Ag nanoparticles, for the uniform and dense Li deposition. The as-designed Ag-embedded MWCNT bucky paper (Ag/MCBP) achieves low Li nucleation overpotentials and high coulombic efficiencies (CEs), owing to the high Li affinity of Ag nanoparticles and 3D electronically conductive, porous architecture of MWCNT. Consequently, the optimized sample of Ag/MCBP-10 delivers a high average CE of 99.31% over 150 cycles at 2 mA cm^{-2} and

4 mAh cm^{-2} in symmetric cells. The Li metal full batteries are configured pairing Li@Ag/MCBP-10 with lithium iron phosphate (LFP), lithium manganese iron phosphate (LMFP), and nickel-rich $\text{LiNi}_{0.8}\text{Co}_{0.1}\text{Mn}_{0.1}\text{O}_2$ (NCM811). The Li@Ag/MCBP-10||LFP full cells retain 95.65% of capacity after 100 cycles at 1C, while the Li@Ag/MCBP-10||LMFP full cells achieve 79.30% of capacity retention after 100 cycles at 0.5C. Moreover, the Li@Ag/MCBP-10||NCM811 full cells, with a high mass loading of NCM811 cathode (22 mg cm^{-2} , 4.4 mAh cm^{-2}) deliver the high specific capacity of $208.74 \text{ mAh g}^{-1}$ at 0.2C rate under harsh condition of ≈ 0.9 neutron-to-proton ratio.

1. Introduction

Lithium (Li) metal anode has garnered significant attention as a promising energy storage material owing to its theoretical specific capacity (3860 mAh g^{-1}) and the lowest redox potential (-3.04 V vs standard hydrogen electrode) for energy dense batteries.^[1] However, Li metal anodes suffer from dendrite growth caused by uneven Li-ion distribution on the substrate, the instability of the solid electrolyte interphase (SEI) layer, and large volume change (an expansion of $4.8 \mu\text{m}$ per mAh cm^{-2}) during the Li

metal plating/stripping process.^[2–4] In order to resolve the aforementioned issues, various strategies have been investigated, including the modification of electrolyte compositions,^[5] the development of advanced separators,^[6] and the formation of artificial SEI.^[7] These extensive studies have been conducted to address the issues of Li metal anodes; however, the operation of Li metal batteries under practical conditions remains a significant challenge.^[8] In the case of lithium metal batteries, the N/P ratio (defined as the anode-to-cathode capacity ratio) is also a critical factor for achieving practical cell operation.^[9,10] Although a higher N/P ratio can enhance cell stability, it inevitably leads to a significant reduction in both gravimetric and volumetric energy density due to the presence of excess lithium reservoirs.^[11,12] Therefore, extensive research efforts have been devoted to developing lithium metal batteries with near-zero N/P ratios to maximize energy density.^[13] In low N/P ratio cell systems, cell failure is predominantly attributed to active lithium depletion rather than electrolyte depletion during repeated cycling.^[14] Consequently, promoting highly reversible lithium deposition and stripping at the current collector surface plays a key factor in enabling stable cycles under low N/P ratio conditions.^[15]

Recently, 3D hosting materials that can accommodate Li metals have been developed to resolve these issues.^[16] 3D hosts can preserve the structure of the electrode and sustain volume expansion and contraction during Li metal plating and stripping processes.^[17] Furthermore, 3D hosts can also reduce the effective current density owing to a large surface area, which, in turn, extends the Sand's time and suppresses the growth of Li dendrites.^[18,19] Representative examples include porous metals, including Cu,^[20] Ni,^[21] etc., and carbonaceous materials, such as reduced graphene oxide,^[1,22] carbon nanotube,^[23] carbon fiber,^[17] etc. In particular, carbonaceous materials are beneficial for 3D hosts owing to their large surface area, high electrical

J. S. Kim, C. Park, D. H. Min, T. Kang, J. S. Byun, S. Kim, W. I. Kim, H. G. Cho, H. C. Kim, M. J. Kim, H. S. Park

School of Chemical Engineering

Sungkyunkwan University (SKKU)

Suwon 16419, Republic of Korea

E-mail: phs0727@skku.edu

H. S. Park

Department of Health Sciences and Technology

Samsung Advanced Institute for Health Sciences and Technology (SAIHST)

Sungkyunkwan University

2066, Seoburo, Jangan-gu, Suwon 440-746, Republic of Korea

H. S. Park

SKKU Advanced Institute of Nano Technology (SIANT)

Sungkyunkwan University

2066, Seoburo, Jangan-gu, Suwon 440-746, Republic of Korea

H. S. Park

SKKU Institute of Energy Science and Technology (SIEST)

Sungkyunkwan University

2066, Seoburo, Jangan-gu, Suwon 440-746, Republic of Korea



Supporting information for this article is available on the WWW under <https://doi.org/10.1002/batt.202500353>



© 2025 The Author(s). *Batteries & Supercaps* published by Wiley-VCH GmbH. This is an open access article under the terms of the Creative Commons Attribution License, which permits use, distribution and reproduction in any medium, provided the original work is properly cited.

conductivity, electrochemical, thermal, and mechanical stabilities, and diverse morphologies, and chemistries.^[1,22,24] However, these approaches based on 3D carbon hosts are limited by insufficient Li-ion distribution capabilities onto the substrate surface due to intrinsic lithiophobicity, leading to uneven and nonuniform Li deposition. Furthermore, the excessive surface area of the 3D carbon host was attributed to parasitic reactions with the electrolyte upon cycling, which could drastically degrade the cell performance.^[25,26] Accordingly, several approaches have been developed to improve the lithiophilicity of 3D carbon hosts.^[27,28] Examples include the introduction of metal oxides^[29] or metal particles^[30] into the 3D hosts for the improved lithiophilicity. However, it is still difficult to uniformly distribute these lithiophilic sites onto the 3D surface, which results in the formation of dead Li and dendrites.^[31] Moreover, a time- and cost-intensive process under high vacuum conditions is required for achieving a uniform distribution of lithiophilic sites.^[32]

Herein, we demonstrate a 3D Li host of lithiophilic Ag nanoparticles uniformly embedded into multi-walled carbon nanotubes (MWCNT) bucky paper (Ag/MCBP) scaffolds for the stable Li metal batteries. Along with the uniform and dense Li deposition, the Ag/MCBP exhibited significantly reduced nucleation overpotential and improved coulombic efficiency (99.08% over 230 cycles), much better than those of MCBP (98.92% over 110 cycles) and Cu foil (97.89% over 70 cycles). Under the practical conditions, Ag/MCBP-10 maintained higher cyclic stability (99.31% over 150 cycles) than those of MCBP and Cu foil. The Li@Ag/MCBP-10||lithium iron phosphate (LFP) full cells retained 80.00% of initial capacity over 170 cycles, outperforming MCBP (100 cycles) and Cu foil (18 cycles). Moreover, the potential of Ag/MCBP-10 as Li hosting materials was further demonstrated by evaluating the electrochemical performances of full cells paired with lithium manganese iron phosphate (LMFP) and high-mass-loading nickel-rich $\text{LiNi}_{0.8}\text{Co}_{0.1}\text{Mn}_{0.1}\text{O}_2$ (NCM811) cathodes. This work provides the rational design of 3D Li hosts based on the Ag-embedded carbon nanotube bucky papers for energy dense Li metal batteries.

2. Results and Discussion

Figure 1a represents a schematic illustration of the fabrication of Ag-embedded MWCNT bucky paper. The MWCNT was dispersed in water with silver nitrate and carboxymethyl cellulose (CMC) surfactant as followed by doctor blade pasting and drying at 80 °C. After drying, the film was peeled off from the polyester (PET) film to obtain bucky paper. Lastly, the Ag nanoparticles were nucleated and grown by heat treatment under an H₂ atmosphere at 600 °C. As shown in the optical image of Figure 1b, the resulting Ag/MCBP-10 was in the form of free-standing paper with mechanical integrity. During a fabrication process, the thickness of bucky papers was reduced using a heating roll press to achieve a similar thickness to commercially available Cu foils. The cross-sectional scanning electron microscope (SEM) image confirmed that the thickness of Ag/MCBP-10 was estimated as 20 µm (Figure 1c).

Transmission electron microscopy (TEM) analyses were conducted to investigate the size and distribution of the Ag nanoparticles on the surface of Ag/MCBP-10. The pristine MCBP shows the macroporous structure internetworked by MWCNTs with an outer diameter of 20–30 nm (Figure S1, Supporting Information). The Ag nanoparticles with the coating layer of carbon were tightly embedded onto the surface of MWCNT as shown in Figure 1d (Figure S2, Supporting Information). This carbon layer with a thickness of 1 nm was derived from the decomposition and carbonization of CMC used for the preparation of the MWCNT dispersion. These carbon-coated Ag nanoparticles were well discretized in the form of single particles without any aggregation and distributed over the whole region of MCBP (Figure 1e).

Elemental mapping images of energy dispersive X-ray spectroscopy (EDS) were further collected to verify the distribution of Ag nanoparticles. The random distribution of Ag nanoparticles on the surface of MWCNT without significant aggregation was confirmed by observing the signal of Ag element (Figure 1f). A comparison of Ag/MCBP-10 and MCBP EDS mapping images demonstrated that Ag nanoparticles were successfully introduced using silver nitrate as the Ag precursor (Figure 1f and S3, Supporting Information). Additionally, the signal of Ag nanoparticles overlapped with that of carbon, which further supports the existence of carbon coating layers (Figure 1f,g). Furthermore, TEM analyses were performed to investigate the change in the sizes of Ag nanoparticles varying the content of silver precursor. The samples were denoted as Ag/MCBP-5 for 5 wt%, Ag/MCBP-10 for 10 wt%, and Ag/MCBP-15 for 15 wt% according to the content of Ag precursor relative to MWCNT. As the amount of added silver nitrate increased, the sizes of the Ag nanoparticles also increased from 10 to 50 nm (Figure S4, Supporting Information).^[33] The content of Ag nanoparticles in Ag/MCBP was estimated as a function of the amount of the Ag precursor, obtaining thermogravimetric analysis (TGA) curves measured under an air atmosphere at a heating rate of 5 °C min⁻¹. As shown in TGA curves (Figure S5, Supporting Information), the weight percentages of Ag nanoparticles increased with the amount of added silver nitrate, which increased about 2.2, 5.3, and 6.3 wt% for Ag/MCBP-5, Ag/MCBP-10, and Ag/MCBP-15, respectively. Moreover, the decomposition temperatures of Ag/MCBP-5, Ag/MCBP-10, and Ag/MCBP-15 were lowered compared to that of MCBP due to the catalytic effect of Ag nanoparticles on the thermal decomposition of the MWCNT.^[34]

X-ray diffraction (XRD) analyses were conducted to confirm the crystalline structures of Ag nanoparticles embedded in the Ag/MCBP (Figure 2a). A relatively broad peak corresponding to the (002) plane of MWCNT was observed at around 26°,^[35] indicating that the crystallinity of the MWCNT was preserved during the fabrication of the bucky papers. Additionally, peaks at 44.5° and 51.9° are assigned to the (100) and (004) planes of MWCNT.^[36] In a different manner to the spectrum of MCBP, new peaks of Ag/MCBP-5, Ag/MCBP-10, and Ag/MCBP-15 appeared at 38.1°, 44.3°, 64.4°, and 77.4°, which indicates the face-centered cubic crystalline structure of Ag nanoparticles (ICDD #03-065-2871).^[37] Furthermore, these peaks are assigned to the (111), (200), (220), and (311) crystalline planes of Ag, respectively. When the content of silver nitrate increased, the peak intensity of the (002) plane of

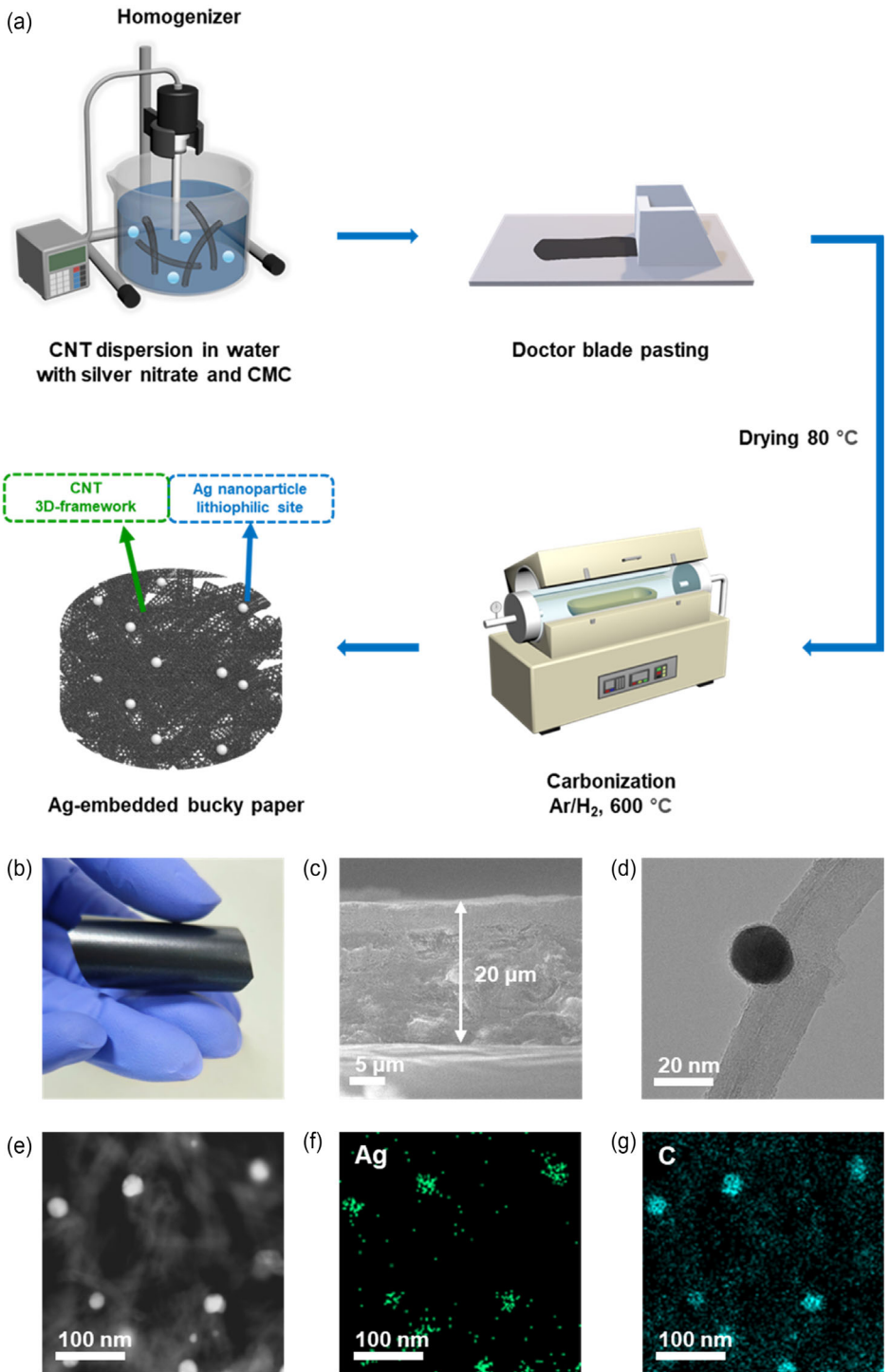


Figure 1. a) Schematic illustration for synthesis procedure of Ag/MCBP. b) Optical image of Ag/MCBP-10. c) Cross-sectional SEM image of Ag/MCBP-10. d) TEM, e) HADDF-STEM, and f,g) corresponding STEM-EDS mapping images of Ag/MCBP-10.

MWCNT was relatively lowered, while the peak intensity of the (111) plane of Ag nanoparticles increased.

The N₂ sorption/desorption isotherms were obtained to investigate the specific surface areas and the pore size distributions of Ag/MCBP-5, Ag/MCBP-10, Ag/MCBP-15, and MCBP (Figure 2b). All samples exhibited type II isotherms due to the presence of macropores with no hysteresis.^[38] The specific surface areas derived from Brunauer–Emmett–Teller (BET) decreased

from 94.38 m² g⁻¹ (MCBP) to 82.35 m² g⁻¹ (Ag/MCBP-5), 80.58 m² g⁻¹ (Ag/MCBP-10), and 78.25 m² g⁻¹ (Ag/MCBP-15) as the content of Ag nanoparticles increased. As evaluated by the BJH pore size distribution of the samples (Figure S6, Supporting Information), the pore volume decreased from 1.05 cm³ g⁻¹ (MCBP) to 0.89 cm³ g⁻¹ (Ag/MCBP-5), 0.80 cm³ g⁻¹ (Ag/MCBP-10), and 0.71 cm³ g⁻¹ (Ag/MCBP-15) when the content of Ag nanoparticles increased in a similar manner to

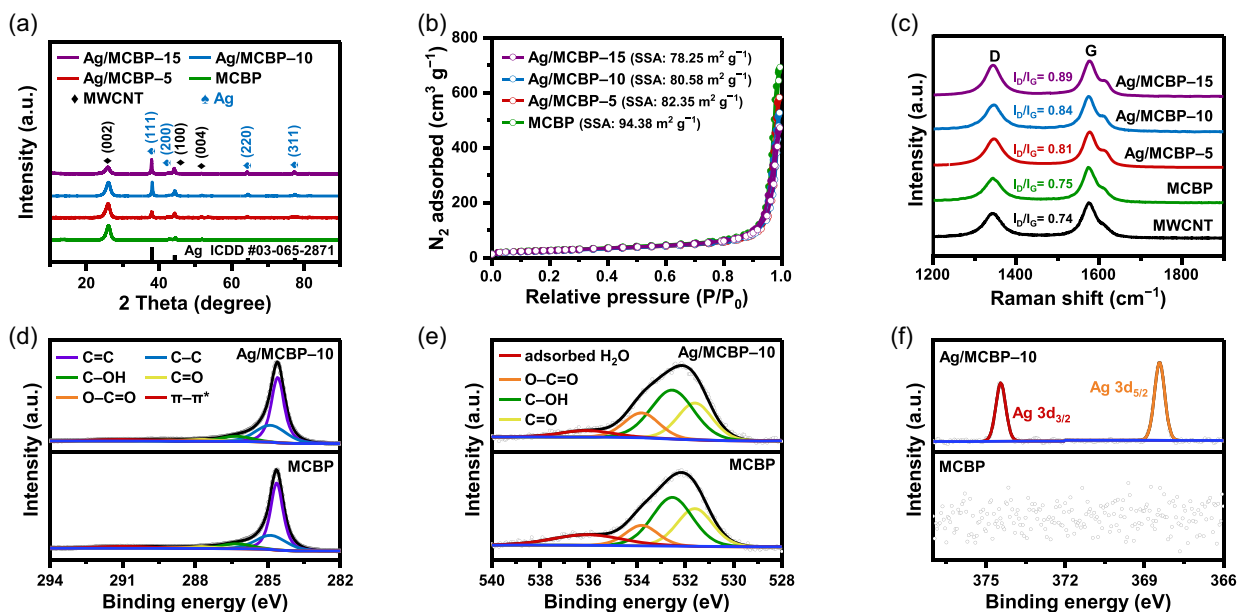


Figure 2. a) XRD spectra, b) N_2 sorption/desorption isotherms, and c) Raman spectra of Ag/MCBP-5, Ag/MCBP-10, Ag/MCBP-15, and MCBP. High-resolution XPS d) C 1s, e) O 1s, and f) Ag 3d spectra of Ag/MCBP-10 and MCBP.

the specific surface area. Consequently, this reduction of specific surface area and pore volume of MCBP was attributed to the pore blocking of Ag particles embedded (Table S1, Supporting Information), as previously reported.^[39]

The electronic structure of Ag/MCBP was characterized using Raman spectroscopy (Figure 2c). Specifically, two peaks were observed at 1344 and 1574 cm⁻¹, corresponding to the D and G bands of MWCNT, respectively.^[40] The intensity ratio of D and G bands (I_D/I_G) indicates the degree of defects of MWCNT.^[41] The I_D/I_G ratios of MWCNT and MCBP were 0.74 and 0.75, respectively, indicating the preservation of intrinsic conjugated structure in the formation process of bucky paper. After the incorporation of Ag nanoparticles into MCBP, the I_D/I_G ratio increased to 0.81, 0.84, and 0.89 for Ag/MCBP-5, Ag/MCBP-10, and Ag/MCBP-15, respectively. The degree of defects for MWCNTs increased due to the existence of Ag nanoparticles deposited onto the surface of Ag/MCBP, which disrupted the C=C bonding of sp^2 graphitic carbon.^[42]

The chemical structure and status of the Ag/MCBP were further investigated using X-ray photoelectron spectroscopy (XPS) as shown in Figure 2d-f and S7, Supporting Information. The high-resolution C 1s spectra of Ag/MCBP-5, -10, -15, and MCBP were deconvoluted into six peaks corresponding to C=C (284.6 eV), C-C (284.8 eV), C-OH (286.3 eV), C=O (287.8 eV), O-C=O (289.3 eV), and $\pi-\pi^*$ (290.9 eV).^[43] The chemical bond between Ag and carbon (Ag-C at 284.0 eV) was not observed in the C 1s spectra.^[44] The chemical bond between Ag and MCBP observed in the C 1s spectra was further confirmed in the O 1s spectra (Figure 2e). The O 1s spectra were deconvoluted into four peaks corresponding to C=O (531.6 eV), C-OH (532.5 eV), O-C=O (533.8 eV), and adsorbed H₂O (536.1 eV).^[45] No peak related to the Ag-O bond at 528.4 eV was found, indicating that Ag was not existing in an oxidized form.^[46] As shown

in the Ag 3d spectra in Figure 2f, no peak was observed for the MCBP, whereas two peaks were captured for Ag/MCBP-5, Ag/MCBP-10, and Ag/MCBP-15 (Figure S5e,f, Supporting Information). Two peaks located at 374.4 and 368.4 eV were assigned to Ag 3d_{5/2} and Ag 3d_{3/2}, respectively, corresponding to the metallic Ag⁰ state,^[47] which was consistent with no detection of Ag-O bond in the O 1s spectra. This finding means that Ag⁺ from silver nitrate was successfully reduced into Ag nanoparticles during the heat treatment indicating no formation of chemical bonding between Ag and MCBP.

To verify the superiority of the Ag/MCBP for the Li metal hosts, Li|Ag/MCBP, Li|MCPB, and Li|Cu half cells were tested in LiFSI/DME/1,1,2,2-tetrafluoroethyl 2,2,3,3-tetrafluoropropyl ether) electrolytes (1/1/2/3 molar ratio). According to previous research,^[48] the morphology of deposited lithium significantly influences CE. When lithium deposits form denser and bulkier structures, the specific surface area exposed to the electrolyte decreases, consequently enhancing CE by reducing side reactions. Additionally, reduced nucleation overpotential lowers the energy barrier for lithium deposition,^[49] promoting dendrite-free, dense, and bulkier lithium growth, further improving CE.^[50] Therefore, we first measured the nucleation overpotential and CE and validated the superiority of Ag/MCBP. Li nucleation overpotential, which is caused by the energy barrier required for nucleation, was measured at 0.5 mA cm⁻² with a specific capacity of 1 mAh cm⁻² to evaluate the lithophilicity of the substrate (Figure 3a and S8, Supporting Information). The nucleation overpotential for Ag/MCBP-5, Ag/MCBP-10, Ag/MCBP-15, MCBP, and Cu were determined as 6, 9, 13, 19, and 53 mV, respectively, indicating that the nucleation overpotential was lowered by lithophilic Ag nanoparticles.^[51] For the optimal composition of Ag nanoparticles, CEs of Ag/MCBP-5, Ag/MCBP-10, and Ag/MCBP-15 were measured at 2 mA cm⁻² and 2 mAh cm⁻² (Figure S9,

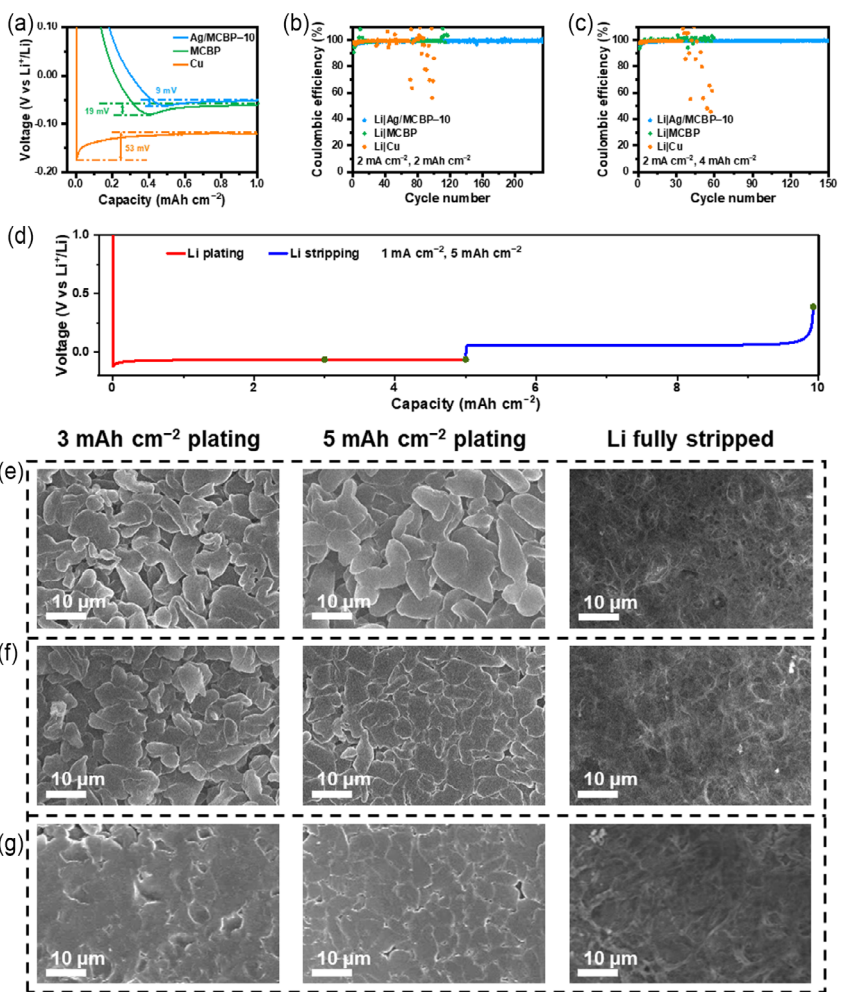


Figure 3. a) Voltage-capacity profiles of Li plating on Ag/MCBP-10, MCBP, and Cu. b) CE of Ag/MCBP-10, MCBP, and Cu. b) at a current density of 2 mA cm^{-2} with a capacity of 2 mAh cm^{-2} and c) at a current density of 2 mA cm^{-2} with a capacity of 4 mAh cm^{-2} . d) Li plating/stripping voltage profile at 1 mA cm^{-2} for 5 mAh cm^{-2} . Top-view SEM images of e) Cu, f) MCBP, and g) Ag/MCBP-10 after plating 3 mAh cm^{-2} and fully stripping.

Supporting Information). Among three samples, Ag/MCBP-10 exhibited more stable CEs and longer cycle stability of 230 cycles compared to 77 cycles of Ag/MCBP-5 and 128 cycles of Ag/MCBP-15. Furthermore, Ag/MCBP-10 achieved a higher average CE of 99.08% than 98.84 and 98.88% of Ag/MCBP-5 and Ag/MCBP-15, respectively. For Ag/MCBP-5, the low Ag content may have hindered the effective utilization of the intrinsic lithiophilicity of Ag nanoparticles, resulting in a low CE. During cell operation, Ag nanoparticles reacted with Li to form Li-Ag alloys, which induced volume expansion.^[52] Considering that the content of Ag nanoparticles for Ag/MCBP-15 was larger than those in Ag/MCBP-5 and Ag/MCBP-10, volume expansion caused by more Ag nanoparticles led to fractures in the 3D carbon host, resulting in poor electrochemical performance.^[53] Despite the lower nucleation overpotential of Ag/MCBP-15 than that of Ag/MCBP-10, the former achieved lower CEs. To investigate this phenomenon in detail, the local hardness of MCBP and Ag/MCBP were evaluated using the nanoindentation method. As shown in Figure S10, Supporting Information, the load applied to the nanoindenter tip was measured as a function of local displacement. Based on these measurements, the local hardness values were

determined to be 48.196 MPa for MCBP, and increased to 54.498 and 59.566 MPa for Ag/MCBP-5 and Ag/MCBP-10, respectively. This improvement is attributed to the role of Ag nanoparticles as energy dissipation points that reinforce the mechanical integrity of the composite structure.^[54] However, with Ag/MCBP-15 content, the hardness sharply decreased to 11.866 MPa, likely due to nanoparticle agglomeration, which weakened the mechanical property of the composite.^[53a,55] Fracture of the 3D host occurs during lithiation due to reduced mechanical robustness, especially under the volume expansion from Li-Ag alloy formation. This leads to a noticeable decline in CE. Based on these CE data, Ag/MCBP-10 was chosen as the optimal sample for additional electrochemical measurements.

The reversibility of Ag/MCBP-10 for Li plating and stripping was further investigated compared with the CEs of MCBP and Cu. As shown in Figure 3b, Ag/MCBP-10 exhibited the highest CE of 99.08% over 230 cycles at 2 mA cm^{-2} with a capacity of 2 mAh cm^{-2} . This value of Ag/MCBP-10 was much greater than 98.70% of Cu after 80 cycles and 98.92% of MCBP after 120 cycles. At the high capacity of 4 mAh cm^{-2} at 2 mA cm^{-2} , the average CE of Ag/MCBP-10 was 99.31% for 150 cycles, which was much

greater than 99.07 and 98.52% of MCBP and Cu over 30 cycles, respectively (Figure 3c).

The Nyquist plots of Ag/MCBP-10, MCBP, and Cu were collected using electrochemical impedance spectroscopy (EIS) before and after 5 cycles at 0.5 mA cm^{-2} in the voltage range from 0.01 to 1.0 V (Figure S11, Supporting Information). Before cycling, Ag/MCBP-10 exhibited a lower charge-transfer resistance (R_{ct}) value of 71.9Ω than 169.8 and 897.9Ω of MCBP and Cu, respectively, which was derived from the diameter of the semicircle in the middle to high frequency region. After 5 cycles under identical condition, the R_{ct} value of Ag/MCBP-10 was 9.8Ω , lower than 11.5 and 95.5Ω of MCBP and Cu, respectively. This lowest value of R_{ct} reflects the synergistic effect of the embedded Ag nanoparticles and the interconnected porous MWCNT bucky paper.

The Li morphologies deposited on the surfaces of Ag/MCBP-10, MCBP, and Cu were investigated by obtaining top-view SEM images after electrochemical Li deposition of 3 and 5 mAh cm^{-2} and full stripping in the Li|Ag/MCBP-10, Li|MCBP, and Li|Cu cell configurations. Subsequently, the surface of deposited Li was mildly washed with DME before SEM measurements. Figure 3d shows the galvanostatic discharge/charge (GCD) curve for 5 mAh cm^{-2} of Li plating

at a current density of 1 mA cm^{-2} , as followed by 5 mAh cm^{-2} of Li stripping at the same current density. To examine the growth morphology of lithium, SEM analyses were conducted by varying the deposition capacity during lithium plating (Figure 3f-h). At a Li plating capacity of 3 mAh cm^{-2} , Ag/MCBP-10 exhibited the densely packed Li with minimal voids owing to the lithiophilicity of Ag nanoparticles,^[56] whereas MCBP and Cu revealed many void spaces indicating nonuniform Li deposition and rough surface. When the Li plating capacity increased to 5 mAh cm^{-2} , some of the previously vacant spaces for Ag/MCBP-10 became more densely filled. On the other hand, MCBP showed more packed Li granules, but more voids still existed compared to those of Ag/MCBP-10, which further confirms the importance of Ag nanoparticles for uniform and dense Li deposition.^[48] Furthermore, Li deposits of Cu still show many voids.

Symmetric cells based on Li predeposited electrodes were assembled to examine the cyclic stabilities at 2 mA cm^{-2} and 2 mAh cm^{-2} as well as at 5 mA cm^{-2} and 1 mAh cm^{-2} . Prior to assembling the symmetric cells, a Li capacity of 6 mAh cm^{-2} at 1 mA cm^{-2} was predeposited onto the Ag/MCBP-10, MCBP, and Cu, resulting in electrodes referred to as Li@Ag/MCBP-10, Li@MCBP, and Li@Cu, respectively. As shown in Figure 4a,

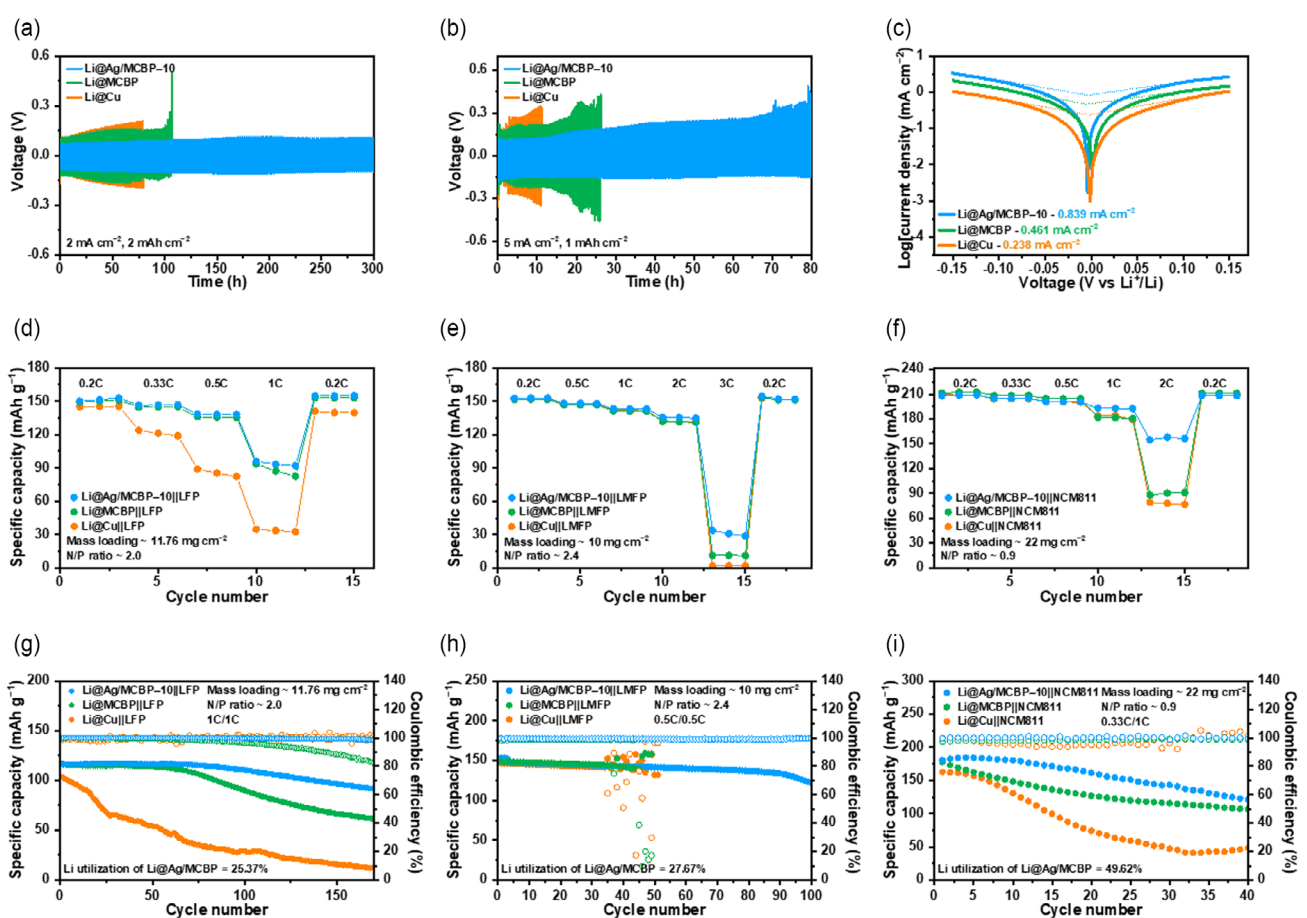


Figure 4. Cycling stability of symmetric cells of Li@Ag/MCBP-10, Li@MCBP, and Li@Cu a) at a current density of 2 mA cm^{-2} with a capacity of 2 mAh cm^{-2} b) at a current density of 5 mA cm^{-2} with a capacity of 1 mAh cm^{-2} c) Tafel curves of Li@Ag/MCBP-10, Li@MCBP, and Li@Cu symmetric cells. Full-cells rate performance of Li@Ag/MCBP-10, Li@MCBP, and Li@Cu anode fabricated with d) LFP cathode, e) LMFP cathode, and f) NCM811 cathode. Full-cells cycle retentions of Li@Ag/MCBP, Li@MCBP, and Li@Cu anode fabricated with g) LFP cathode with 1C charge/1C discharge, h) LMFP cathode with 0.5C charge/0.5C discharge, and i) NCM811 cathode with 0.33C charge/1C discharge.

Li@Ag/MCBP-10||Li@Ag/MCBP-10 symmetric cells achieved a lower voltage hysteresis of 108 mV than 129 and 146 mV of the Li@MCBP and Li@Cu-based ones, respectively, which is consistent with the trend about the R_{ct} values (Figure S11, Supporting Information). Moreover, Li@Ag/MCBP-10||Li@Ag/MCBP-10 symmetric cells achieved a longer cycle life for over 300 h and continued, exceeding 107 and 79 h for Li@MCBP and Li@Cu-based cells, respectively. The cycle stability of Li@Ag/MCBP-10 based symmetric cell was evaluated under harsher conditions and compared with Li@MCBP and Li@Cu-based ones. The long-term stability of Li@Ag/MCBP-10 based cells at 5 mA cm⁻² and 1 mAh cm⁻² was preserved up to 70 h, better than 26 and 11 h of Li@MCBP, and Li@Cu, respectively (Figure 4b). Furthermore, Li@Ag/MCBP-10 showed lower voltage hysteresis of 150 mV than 180 and 302 mV of Li@MCBP and Li@Cu, respectively.

The Li plating and stripping kinetics of the electrodes in symmetric cells were evaluated by Tafel slope. The Tafel slopes were obtained by measuring cyclic voltammetry curves in a potential window of -0.15 to 0.15 V at a scan rate of 2 mV s⁻¹ (Figure S12, Supporting Information). As shown in Figure 4c, the Li@Ag/MCBP-10 electrodes exhibited a higher exchange current density of 0.839 mA cm⁻² than those of Li@MCBP (0.461 mA cm⁻²) and Li@Cu (0.238 mA cm⁻²), indicating the faster charge-transfer kinetics.

Owing to the facilitated ion transport kinetics and reduced interfacial charge-transfer resistance, the practical applicability of the Ag/MCBP host was evaluated through full cell measurements. Full cell measurements were conducted by assembling 2032-type coin cells of Li@Ag/MCBP-10 (deposited up to 4 mAh cm⁻²) with various cathodes. As shown in Figure 4d, the electrochemical performance was initially evaluated using a high mass loading of LFP cathode (11.76 mg cm⁻², N/P ratio of ≈2.0). The Li@Ag/MCBP-10||LFP full cells achieved the higher specific capacity of 153.0 mAh g⁻¹ at 0.2C rate compared to 150.2 and 145.5 mAh g⁻¹ of Li@MCBP||LFP and bare Li@Cu||LFP, respectively. When the rates increased up to 1C, the specific capacity of 95.8 mAh g⁻¹ for the Li@Ag/MCBP-10||LFP cell became much higher than 82.5 mAh g⁻¹ for the Li@MCBP||LFP cell. On the other hand, the bare Li@Cu||LFP achieved a very low capacity of 34.9 mAh g⁻¹ at the same 1C rate.

The LMFP is considered the promising olivine-type cathode material owing to its higher electrode potential compared to LFP.^[57] As shown in Figure 4e, the Li@Ag/MCBP-10||LMFP full cells with a high mass loading of LMFP cathode (10 mg cm⁻², N/P ratio of ≈2.4) achieved a slightly higher specific capacity of 154.62 mAh g⁻¹ at 0.2C rate, compared to 153.33 and 152.74 mAh g⁻¹ of Li@MCBP||LMFP and bare Li@Cu||LMFP, respectively. When the rates increased up to 3C, the specific capacity of 33.71 mAh g⁻¹ for the Li@Ag/MCBP-10||LFP cell became much higher than 11.32 mAh g⁻¹ for the Li@MCBP||LFP cell. On the other hand, the specific capacity of bare Li@Cu||LFP was 1.85 mAh g⁻¹, nearly negligible due to the poor rate capability.

The NCM811 cathode was applied for energy dense Li metal full batteries owing to its high reversible capacity and operating voltage.^[58] For the practical application, Li@Ag/MCBP-10||NCM811 full cells with a high mass loading of NCM811 cathode

(22 mg cm⁻², 4.4 mAh cm⁻²) were tested under harsh conditions, where the N/P ratio was ≈0.9. As depicted in Figure 4f, the Li@Ag/MCBP-10||NCM811 full cells achieved the high specific capacity of 208.74 mAh g⁻¹ at 0.2C rate. When the current rates increased up to 2C, the specific capacity of the Li@Ag/MCBP-10||NCM811 cell was preserved up to 158.13 mAh g⁻¹, much higher than 88.18 and 76.61 mAh g⁻¹ of the Li@MCBP||LFP and Li@Cu||NCM811 cells, respectively, indicating high rate capability.

The cell performance of Li@Ag/MCBP-10||LFP was further evaluated by measuring cycling stability as shown in Figure 4g. The high capacity retention of 95.65% with reference to its initial capacity, which was much higher than 76.82 and 27.66% of Li@MCBP||LFP and bare Li@Cu||LFP cells, respectively, was achieved after 100 cycles at 1C charge/discharge rate. The decrease in capacity retention of bare Li@Cu||LFP and Li@MCBP||LFP is attributed to the accumulation of dead Li and the consumption of the electrolyte during repeated cycling.^[59] As shown in Figure S13, Supporting Information, the Li@Ag/MCBP-10||LFP cell exhibited a capacity retention of 25.99% after 500 cycles. This performance was an improvement over the Li@MCBP||LFP cell, which showed a retention of 13.71% under the same conditions. In contrast, the Li@Cu||LFP cell experienced a rapid capacity fade, with its retention dropping to 8.3% after 300 cycles. Consequently, the Li@Ag/MCBP-10||LFP cell demonstrated the most outstanding cycling stability even over an extended 500 cycles. As shown in Figure 4h, the Li@Cu||LMFP and Li@MCBP||LMFP full cells exhibited capacity fluctuations at the 40th and 50th cycle, respectively, as followed by rapid cell failure. In contrast, the Li@Ag/MCBP-10||LMFP full cell delivered a higher capacity retention of 79.3% after 100 cycles, demonstrating significantly improved cycling stability owing to the reversible Li deposition.^[60] Furthermore, the capacity retention of Li@Ag/MCBP-10||NCM811 full cell was 66.96% at the 40th cycle, higher than 29.96 and 60.89% for Li@Cu||NCM811 and Li@MCBP||NCM811, respectively, as shown in Figure 4i. To further elucidate the capacity fading in the Li@Ag/MCBP-10||NCM811 full cells, a systematic postmortem analysis was conducted, with a particular focus on the degradation of the Li@Ag/MCBP-10 anodes. In anode-free full cells with N/P ratios below 1, it is widely recognized that the primary cause of cell failure is the depletion of the lithium reservoir, rather than electrolyte consumption.^[61] However, the contribution of cathode degradation to the overall performance loss cannot be disregarded. Therefore, focused ion beam-scanning electron microscopy was employed to examine the structural integrity of the NCM811 secondary particles after cycling. This approach was guided by previous reports that highlighted microcracking as a critical contributor to long-term performance decay in layered transition metal oxides such as NCM811 and NCA.^[62] As shown in Figure S14, Supporting Information, microcracks in the secondary particles were observed in all tested configurations including Li@Cu||NCM811, Li@MCBP||NCM811, and Li@Ag/MCBP-10||NCM811. These observations suggest that cathode microcracking was not the primary cause of the observed capacity fading. To verify that the consumption of the lithium reservoir was the primary failure mode, the full cells were disassembled after cycling and the surface morphology of the Li@Ag/MCBP-10 anode was inspected

using optical images (Figure S15, Supporting Information). Signs of lithium depletion were clearly visible at the consumed sites. Furthermore, to determine whether the Ag nanoparticles remained uniformly dispersed on the Ag/MCBP-10 hosts despite lithium deposition/stripping, SEM images and EDS analyses were performed on the cycled anodes at the consumed site of Li@Ag/MCBP-10. As presented in Figure S16, Supporting Information, Ag nanoparticles remained homogeneously distributed across the Ag/MCBP-10 surfaces, suggesting that neither detachment nor local aggregation occurred during cycling. EIS further corroborated the role of Ag in stabilizing the interfacial resistance during prolonged cycling. As shown in Figure S17, Supporting Information, the diameter of the semicircle in the Nyquist plots for the Li@Ag/MCBP-10||NCM811 cell remained nearly constant between the 1st and 30th cycles. In contrast, the semicircle diameter significantly increased in the Li@Cu and Li@MCBP cells, indicating a progressive rise in interfacial resistance. These results collectively confirm that the Ag/MCBP-10 host effectively regulates the interfacial properties. This regulation mitigates the impedance increase and enables more stable cycling, despite the consumption of the active lithium reservoir. These findings collectively demonstrate that the capacity fading was predominantly caused by the loss of the lithium reservoir.^[61,63]

Moreover, to validate the superiority of the Li@Ag/MCBP-10 host, the electrochemical performances of Li@Ag/MCBP-10||LFP full cells were compared with those of other Li metal full cells based on 3D carbon hosts, with reference to relevant literature reports (Table S2, Supporting Information).^[64] Even under more practical conditions of high mass loading (11.76 mg cm^{-2}) and low N/P ratio (≈ 2.0), the specific capacity and cyclic stability were comparable to those of previous literature. These results further confirmed the synergistic effect of lithophilic Ag nanoparticles and electrically conductive, porous MCBP bucky paper on the reversible Li deposition.

The effect of Ag nanoparticles embedded in the MCBP on the Li deposition was investigated through *in situ* XRD spectroscopy, density functional theory (DFT) calculation, and electrochemical characterization. Considering that the formation of Li alloys enhances lithium-ion diffusivity for the improved reversibility of Li deposition,^[52] the formation of Li–Ag alloy and its lithium-ion diffusion were analyzed.^[65] *In situ* XRD data with the corresponding GCD profile and reference peak of Li–Ag alloy were collected as shown in Figure 5a and S18, Supporting Information. New diffraction peaks appear between 21.0° and 22.5° , indicating the progressive formation of Li–Ag alloys during the initial Li deposition process.^[65,66] Upon lithium stripping, these peaks

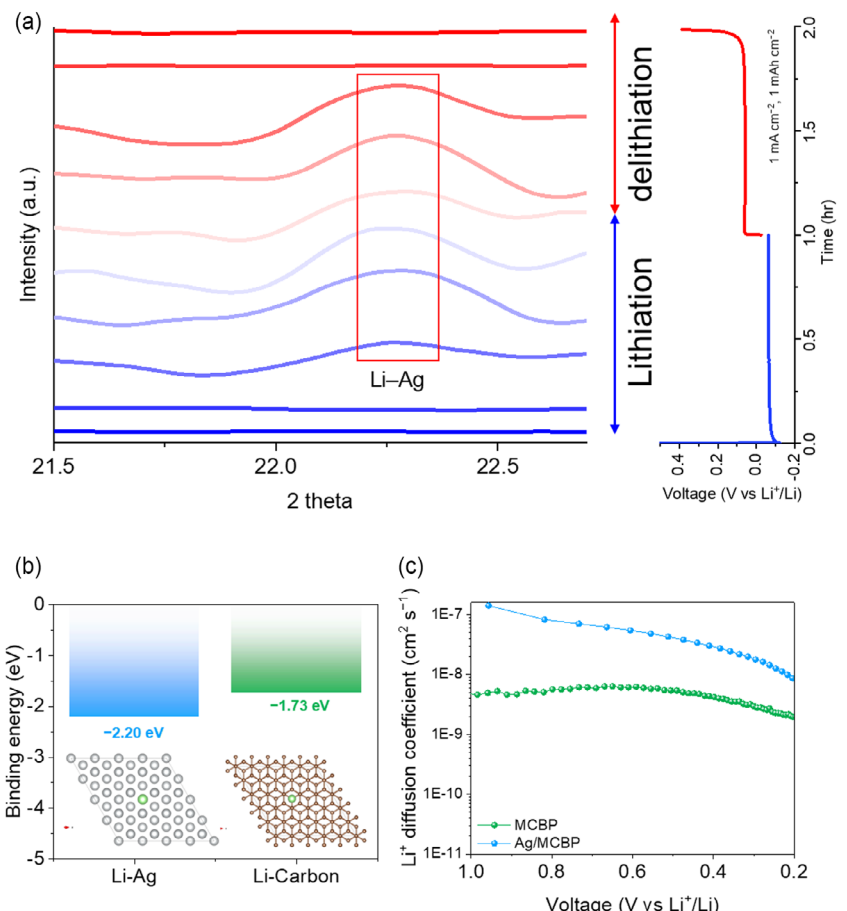


Figure 5. a) *In situ* XRD patterns of Ag/MCBP-10 anode during the lithiation–delithiation cycle under galvanostatic mode at a current density of 1 mA cm^{-2} along with corresponding GCD profile. b) DFT calculation of binding energy to evaluate the lithophilicity of Ag and carbon surfaces. c) Calculated lithium-ion diffusion coefficient based on the GITT curve.

disappeared, which implies that the embedded Ag nanoparticles contributed to the reversible Li deposition through an alloying reaction. The lithiophilicity of these Ag nanoparticles was further confirmed by performing a DFT analysis. Based on previous modeling studies (Figure S19, Supporting Information),^[56,67] the binding energies of Li atoms with Ag and carbon surfaces were calculated. As shown in Figure 5b, the binding energy of Ag with Li was calculated to be -2.20 eV , whereas that with carbon was -1.73 eV . These results indicate that Ag nanoparticles provide higher lithiophilicity compared to carbon, which lowers the nucleation barrier for the formation of Li–Ag alloy and promotes uniform lithium deposition.

To further investigate lithium-ion diffusivity promoted by lithiophilic Ag nanoparticles, galvanostatic intermittent titration technique (GITT) measurements of MCBP|Li and Ag/MCBP|Li cells were performed. GITT profiles were obtained during a lithiation process (Figure S20, Supporting Information), and the corresponding lithium-ion diffusion coefficients were calculated as shown in Figure 5c. A comparison of the Li-ion diffusion coefficients revealed that the Ag/MCBP exhibited approximately one order of magnitude higher values than those of the MCBP, confirming that Ag nanoparticles significantly enhance lithium-ion transport within the host structure.^[60] To further identify the composition of the SEI formed on the anode, XPS analysis was conducted after cycling. As shown in the XPS survey spectrum (Figure S21, Supporting Information), elements corresponding to the SEI composition, including C, N, O, F, S, and Li, were detected, and their atomic contents were calculated accordingly. Based on these atomic contents, our analysis primarily focused on the high-resolution spectra of the inorganic components, F 1s and O 1s, which are critical to the performance of lithium metal batteries (Figure S22 and S23, Supporting Information).^[68] Notably, the Li@Ag/MCBP-10 electrode exhibited the highest atomic percentage of LiF at 6.8%, significantly surpassing that of Li@MCBP (1.45%) and Li@Cu (3.72%). We attribute this to the unique electronic structure of the silver, which likely promotes LiF formation by reducing the energy barrier of the dissociation S–F bond in the FSI^- anion.^[69] In contrast, the composition of Li_2O did not show an appreciable difference among the three electrodes. Therefore, we conclude that in addition to the formation of a Li–Ag alloy, the resulting LiF-rich interface makes a contribution to the enhanced performance of the electrode. These findings demonstrate that the incorporation of Ag nanoparticles not only promotes favorable alloying interactions with lithium but also facilitates lithium-ion transport kinetics, thereby contributing to improved Li deposition for high performance of lithium metal full batteries.

3. Conclusion

In this work, we have demonstrated a 3D Ag/MCBP host of lithiophilic Ag nanoparticles uniformly embedded into MWCNT bucky paper for stable and dendrite-free Li deposition. The uniform and dense Li deposition was attributed to the lithiophilic Ag nanoparticles embedded in 3D electronically conductive, porous architecture of MWCNT as verified by *in situ* XRD spectroscopy,

DFT calculation, and electrochemical characterization. The as-optimized Ag/MCBP-10 achieved the lowest nucleation overpotential and highest CE (99.08% over 230 cycles at 2 mA cm^{-2} and 2 mAh cm^{-2}). Under the practical conditions, Ag/MCBP-10 maintained higher cyclic stability (99.31% over 150 cycles) than those of MCBP and Cu foil. The superiority of Ag/MCBP-10 was further confirmed by configuring Li metal full batteries of Li@Ag/MCBP-10||LFP, Li@Ag/MCBP-10||LMFP, and Li@Ag/MCBP-10||NCM811. Even with high mass loading (11.76 mg cm^{-2}) and low N/P ratio (≈ 2.0), the Li@Ag/MCBP-10||LFP cells achieved the high capacity of 153.0 mAh g^{-1} at 0.2C rate and 80.00% of capacity retention over 170 cycles and cyclic stability, which were comparable to those of state-of-art results. Moreover, the Li@Ag/MCBP-10||LMFP full cells with a high mass loading of LMFP cathode (10 mg cm^{-2} , N/P ratio of ≈ 2.4) achieved a high specific capacity of 154.62 mAh g^{-1} at 0.2C rate and good cyclic stability over 100 cycles. For energy dense Li metal full batteries, the Li@Ag/MCBP-10||NCM811 full cells with a high mass loading of NCM811 cathode (22 mg cm^{-2} , 4.4 mAh cm^{-2}) delivered the high specific capacity of 208.74 mAh g^{-1} at 0.2C rate. This work provides the rational design of 3D Li hosts based on the Ag-embedded carbon nanotube bucky papers for energy dense Li metal full batteries.

Acknowledgements

J.S.K. and C.P. have equally contributed. This work was supported by the National Research Foundation of Korea (NRF) grant funded by the Korea government (MSIT) (no. RS-2023-00217581) and a grant (RS-2024-00470023) from the Materials and Components Technology Development (R&D) Project funded by the Ministry of Trade, Industry and Energy of the Republic of Korea.

Conflict of Interest

The authors declare no conflict of interest.

Data Availability Statement

The data that support the findings of this study are available from the corresponding author upon reasonable request.

Keywords: 3D host · bucky papers · carbon nanotubes · lithium metal anodes · nanoparticles

- [1] a) D. C. Lin, Y. Y. Liu, Z. Liang, H. W. Lee, J. Sun, H. T. Wang, K. Yan, J. Xie, Y. Cui, *Nat. Nanotechnol.* **2016**, *11*, 626; b) J. F. Ding, Y. T. Zhang, R. Xu, R. Zhang, Y. Xiao, S. Zhang, C. X. Bi, C. Tang, R. Xiang, H. S. Park, Q. Zhang, J. Q. Huang, *Green Energy Environ.* **2023**, *8*, 1509.
- [2] D. Luo, M. Li, Y. Zheng, Q. Y. Ma, R. Gao, Z. Zhang, H. Z. Dou, G. B. Wen, L. L. Shui, A. P. Yu, X. Wang, Z. W. Chen, *Adv. Sci.* **2021**, *8*, 2101051.
- [3] S. J. Yang, J. K. Hu, F. N. Jiang, H. Yuan, H. S. Park, J. Q. Huang, *InfoMat* **2023**, *6*, e12512.
- [4] C. Yan, H. Yuan, H. S. Park, J.-Q. Huang, *J. Energy Chem.* **2020**, *47*, 217.
- [5] J. Zheng, G. B. Ji, X. L. Fan, J. Chen, Q. Li, H. Y. Wang, Y. Yang, K. C. DeMella, S. R. Raghavan, C. S. Wang, *Adv. Energy Mater.* **2019**, *9*, 1803774.
- [6] M. S. Gonzalez, Q. Z. Yan, J. Holoubek, Z. H. Wu, H. Y. Zhou, N. Patterson, V. Petrova, H. D. Liu, P. Liu, *Adv. Mater.* **2020**, *32*, 1906836.

- [7] S. F. Liu, X. H. Xia, S. J. Deng, D. Xie, Z. J. Yao, L. Y. Zhang, S. Z. Zhang, X. L. Wang, J. P. Tu, *Adv. Mater.* **2019**, *31*, 1806470.
- [8] Y. Liu, D. Lin, Z. Liang, J. Zhao, K. Yan, Y. Cui, *Nat. Commun.* **2016**, *7*, 10992.
- [9] G. Mu, S. Agrawal, P. Sittisomwong, P. Bai, *Electrochim. Acta* **2022**, *406*, 139878.
- [10] X. Li, R. Zhu, H. Jiang, Y. Yu, W. Wan, X. Li, C. Wang, Y. Huang, *J. Mater. Chem. A* **2022**, *10*, 11246.
- [11] J. Lee, S. H. Jeong, J. S. Nam, M. Sagong, J. Ahn, H. Lim, I. D. Kim, *EcoMat* **2023**, *5*, e12416.
- [12] S. Yuan, T. Kong, Y. Zhang, P. Dong, Y. Zhang, X. Dong, Y. Wang, Y. Xia, *Angew. Chem., Int. Ed. Engl.* **2021**, *60*, 25624.
- [13] Q. Wang, B. Liu, Y. Shen, J. Wu, Z. Zhao, C. Zhong, W. Hu, *Adv. Sci. (Weinh.)* **2021**, *8*, e2101111.
- [14] S. Chen, C. Niu, H. Lee, Q. Li, L. Yu, W. Xu, J.-G. Zhang, E. J. Dufek, M. S. Whittingham, S. Meng, J. Xiao, J. Liu, *Joule* **2019**, *3*, 1094.
- [15] H. Kwon, J. Baek, H.-T. Kim, *Energy Storage Mater.* **2023**, *55*, 708.
- [16] a) H. Ye, S. Xin, Y. X. Yin, J. Y. Li, Y. G. Guo, L. J. Wan, *J. Am. Chem. Soc.* **2017**, *139*, 5916; b) J. Zhao, G. M. Zhou, K. Yan, J. Xie, Y. Z. Li, L. Liao, Y. Jin, K. Liu, P. C. Hsu, J. Y. Wang, H. M. Cheng, Y. Cui, *Nat. Nanotechnol.* **2017**, *12*, 993.
- [17] a) L. Liu, Y. X. Yin, J. Y. Li, N. W. Li, X. X. Zeng, H. Ye, Y. G. Guo, L. J. Wan, *Joule* **2017**, *1*, 563; b) T. T. Zuo, X. W. Wu, C. P. Yang, Y. X. Yin, H. Ye, N. W. Li, Y. G. Guo, *Adv. Mater.* **2017**, *29*, 1700389.
- [18] P. Bai, J. Li, F. R. Brushett, M. Z. Bazant, *Energy Environ. Sci.* **2016**, *9*, 3221.
- [19] B. Hong, H. Fan, X.-B. Cheng, X. Yan, S. Hong, Q. Dong, C. Gao, Z. Zhang, Y. Lai, Q. Zhang, *Energy Storage Mater.* **2019**, *16*, 259.
- [20] a) Q. Li, S. P. Zhu, Y. Y. Lu, *Adv. Funct. Mater.* **2017**, *27*, 1606422; b) H. Zhao, D. N. Lei, Y. B. He, Y. F. Yuan, Q. B. Yun, B. Ni, W. Lv, B. H. Li, Q. H. Yang, F. Y. Kang, J. Lu, *Adv. Energy Mater.* **2018**, *8*, 1800266.
- [21] a) S. S. Chi, Y. C. Liu, W. L. Song, L. Z. Fan, Q. Zhang, *Adv. Funct. Mater.* **2017**, *27*, 1700348; b) Z. Y. Lu, Q. H. Liang, B. Wang, Y. Tao, Y. F. Zhao, W. Lv, D. H. Liu, C. Zhang, Z. Weng, J. C. Liang, H. Li, Q. H. Yang, *Adv. Energy Mater.* **2019**, *9*, 1803186.
- [22] H. Chen, Y. F. Yang, D. T. Boyle, Y. K. Jeong, R. Xu, L. S. de Vasconcelos, Z. J. Huang, H. S. Wang, H. X. Wang, W. X. Huang, H. Q. Li, J. Y. Wang, H. K. Gu, R. Matsumoto, K. Motohashi, Y. Nakayama, K. J. Zhao, Y. Cui, *Nat. Energy* **2021**, *6*, 790.
- [23] Y. Y. Mao, G. R. Li, Y. Guo, Z. P. Li, C. D. Liang, X. S. Peng, Z. Lin, *Nat. Commun.* **2017**, *8*, 14628.
- [24] J.-Y. Hong, E.-H. Sohn, S. Park, H. S. Park, *Chem. Eng. J.* **2015**, *269*, 229.
- [25] M. Bae, Y. Kim, J. Choi, S. Park, L. Lin, T. Yoo, H. Hong, D. Jung, Y. Piao, *Carbon* **2022**, *196*, 663.
- [26] K. Baek, W. G. Lee, E. Im, J. H. Ha, S. Ahn, Y. Kim, Y. Choi, S. J. Kang, *Nano Lett.* **2023**, *23*, 8515.
- [27] A. Huang, Y. Wu, H. Huang, C. Li, Y. Sun, L. Li, S. Peng, *Adv. Funct. Mater.* **2023**, *33*, 2303111.
- [28] T. Yang, L. Li, F. Wu, R. Chen, *Adv. Funct. Mater.* **2020**, *30*, 2002013.
- [29] a) K. Wang, W. Wang, J. Deng, X. Jiang, G. Xu, H. Gong, N. Zhang, D. Li, *J. Alloys Compd.* **2021**, *889*, 161597; b) X. Huo, X. Gong, Y. Liu, Y. Yan, Z. Du, W. Ai, *Adv. Sci. (Weinh.)* **2024**, *11*, e2309254.
- [30] a) K. Yan, Z. Lu, H.-W. Lee, F. Xiong, P.-C. Hsu, Y. Li, J. Zhao, S. Chu, Y. Cui, *Nat. Energy* **2016**, *1*, 16010; b) Y. Liu, J. Sun, X. Hu, Y. Li, H. Du, K. Wang, Z. Du, X. Gong, W. Ai, W. Huang, *Nano Energy* **2022**, *94*, 106883.
- [31] R. Zhang, Y. Li, L. Qiao, D. Li, J. Deng, J. Zhou, L. Xie, Y. Hou, T. Wang, W. Tian, J. Cao, F. Cheng, B. Yang, K. Liang, P. Chen, B. Kong, *Energy Storage Mater.* **2021**, *37*, 123.
- [32] S. H. Wang, J. Yue, W. Dong, T. T. Zuo, J. Y. Li, X. Liu, X. D. Zhang, L. Liu, J. L. Shi, Y. X. Yin, Y. G. Guo, *Nat. Commun.* **2019**, *10*, 4930.
- [33] H. S. Dehsari, A. H. Ribeiro, B. Ersöz, W. Tremel, G. Jakob, K. Asadi, *Crystengcomm* **2017**, *19*, 6694.
- [34] F. Xin, L. Li, *Composites, Part A* **2011**, *42*, 961.
- [35] Y. G. Zhang, G. R. Li, J. Y. Wang, D. Luo, Z. H. Sun, Y. Zhao, A. P. Yu, X. Wang, Z. W. Chen, *Adv. Energy Mater.* **2021**, *11*, 2100497.
- [36] T. Zhang, W. Wang, Z. Ma, L. Bai, Y. Yao, D. Xu, *Int. J. Miner., Metall. Mater.* **2023**, *30*, 1816.
- [37] a) N. Q. Zhang, X. X. Zhang, L. Tao, P. Jiang, C. L. Ye, R. Lin, Z. W. Huang, A. Li, D. W. Pang, H. Yan, Y. Wang, P. Xu, S. F. An, Q. H. Zhang, L. C. Liu, S. X. Du, X. D. Han, D. S. Wang, Y. D. Li, *Angew. Chem., Int. Ed.* **2021**, *60*, 6170; b) A. S. El-Hawary, O. M. Ibrahim, M. H. Kalaba, M. H. El-Sehrawy, M. K. A. Ismail, *Biomass Convers. Biorefin.* **2024**, *15*, 9999.
- [38] K. A. Cychosz, M. Thommes, *Engineering* **2018**, *4*, 559.
- [39] J. S. Yeon, S. Yun, J. M. Park, H. S. Park, *ACS Nano* **2019**, *13*, 5163.
- [40] Z. T. Li, W. N. Zhao, C. Z. Yin, L. Q. Wei, W. T. Wu, Z. P. Hu, M. B. Wu, *ACS Appl. Mater. Interfaces* **2017**, *9*, 44519.
- [41] S. Osswald, M. Havel, Y. Gogotsi, *J. Raman Spectrosc.* **2007**, *38*, 728.
- [42] a) H. Alijani, R. Kaveh, *J. Chem. Technol. Biotechnol.* **2022**, *97*, 2820; b) D. G. Larrude, M. E. H. Maia da Costa, F. L. Freire, C. Estournès, *J. Nanomater.* **2014**, *2014*, 7.
- [43] M. C. Biesinger, *Appl. Surf. Sci.* **2022**, *597*, 153681.
- [44] L. Curet, D. Foix, E. Palomares, L. Billon, A. Viterisi, *Chem. Commun.* **2024**, *60*, 10168.
- [45] a) S. Ben Amor, G. Baud, M. Jacquet, G. Nansé, P. Fioux, M. Nardin, *Appl. Surf. Sci.* **2000**, *153*, 172; b) F. G. Pacheco, A. A. C. Cotta, H. F. Gorgulho, A. P. Santos, W. A. A. Macedo, C. A. Furtado, *Appl. Surf. Sci.* **2015**, *357*, 1015.
- [46] V. K. Kaushik, *J. Electron. Spectrosc.* **1991**, *56*, 273.
- [47] M. R. Salvadori, R. A. Ando, C. A. O. Nascimento, B. Correia, *J. Environ. Sci. Health, Part A: Toxic/Hazard. Subst. Environ. Eng.* **2017**, *52*, 1112.
- [48] M. S. Kim, Z. Zhang, P. E. Rudnicki, Z. Yu, J. Wang, H. Wang, S. T. Oyakhire, Y. Chen, S. C. Kim, W. Zhang, D. T. Boyle, X. Kong, R. Xu, Z. Huang, W. Huang, S. F. Bent, L. W. Wang, J. Qin, Z. Bao, Y. Cui, *Nat. Mater.* **2022**, *21*, 445.
- [49] T. Wu, Y. Wang, W. Zhang, K. Lu, J. Tan, M. Zheng, Y. Xiao, Y. Liu, Y. Liang, *J. Energy Chem.* **2022**, *71*, 324.
- [50] J. Pokharel, A. Cresce, B. Pant, M. Y. Yang, A. Gurung, W. He, A. Baniya, B. S. Lamsal, Z. J. Yang, S. Gent, X. J. Xian, Y. Cao, W. Goddard, K. Xu, Y. Zhou, *Nat. Commun.* **2024**, *15*, 3085.
- [51] X. Y. Li, G. J. Yang, S. M. Zhang, Z. X. Wang, L. Q. Chen, *Nano Energy* **2019**, *66*, 104144.
- [52] Y. Ye, H. Xie, Y. Yang, Y. Xie, Y. Lu, J. Wang, X. Kong, S. Jin, H. Ji, *J. Am. Chem. Soc.* **2023**, *145*, 24775.
- [53] a) Y. G. Lee, S. Fujiki, C. H. Jung, N. Suzuki, N. Yashiro, R. Omoda, D. S. Ko, T. Shiratsuchi, T. Sugimoto, S. Ryu, J. H. Ku, T. Watanabe, Y. Park, Y. Aihara, D. Im, I. T. Han, *Nat. Energy* **2020**, *5*, 348; b) Z. Hou, Y. K. Yu, W. H. Wang, X. X. Zhao, Q. Di, Q. W. Chen, W. Chen, Y. L. Liu, Z. W. Quan, *ACS Appl. Mater. Interfaces* **2019**, *11*, 8148.
- [54] J. S. Kim, J. H. Park, J. W. Hong, H. H. Rana, S. H. Baek, T. H. Kang, S. J. Lee, H. S. Park, *Next Energy* **2023**, *1*, 100066.
- [55] U. Abdullahi, M. A. Maleque, M. Y. Ali, *Mater. Today: Proc.* **2021**, *46*, 6097.
- [56] Y. J. Fang, S. L. Zhang, Z. P. Wu, D. Y. Luan, X. W. Lou, *Sci. Adv.* **2021**, *7*, eabg3626.
- [57] L. Yang, W. Deng, W. Xu, Y. Tian, A. Wang, B. Wang, G. Zou, H. Hou, W. Deng, X. Ji, *J. Mater. Chem. A* **2021**, *9*, 14214.
- [58] H. Maleki Kheimeh Sari, X. Li, *Adv. Energy Mater.* **2019**, *9*, 1901597.
- [59] B. Moorthy, R. Ponraj, J. H. Yun, J. E. Wang, D. J. Kim, D. K. Kim, *ACS Appl. Energy Mater.* **2020**, *3*, 11053.
- [60] H. Zhang, S. Ju, G. Xia, X. Yu, *Sci. Adv.* **2022**, *8*, eabl8245.
- [61] J. Liu, Z. Bao, Y. Cui, E. J. Dufek, J. B. Goodenough, P. Khalifah, Q. Li, B. Y. Liaw, P. Liu, A. Manthiram, Y. S. Meng, V. R. Subramanian, M. F. Toney, V. V. Viswanathan, M. S. Whittingham, J. Xiao, W. Xu, J. Yang, X.-Q. Yang, J.-G. Zhang, *Nat. Energy* **2019**, *4*, 180.
- [62] U.-H. Kim, L.-Y. Kuo, P. Kaghazchi, C. S. Yoon, Y.-K. Sun, *ACS Energy Lett.* **2019**, *4*, 576.
- [63] C. Niu, D. Liu, J. A. Lochala, C. S. Anderson, X. Cao, M. E. Gross, W. Xu, J.-G. Zhang, M. S. Whittingham, J. Xiao, J. Liu, *Nat. Energy* **2021**, *6*, 723.
- [64] a) Z. Du, W. Guan, C. He, Y. Liu, W. Ai, *Energy Storage Mater.* **2024**, *65*, 103191; b) X. Wang, Z. Chen, K. Jiang, M. Chen, S. Passerini, *Adv. Energy Mater.* **2024**, *14*, 2304229.
- [65] S. Jin, Y. Ye, Y. Niu, Y. Xu, H. Jin, J. Wang, Z. Sun, A. Cao, X. Wu, Y. Luo, H. Ji, L. J. Wan, *J. Am. Chem. Soc.* **2020**, *142*, 8818.
- [66] A. Dębski, S. Terlicka, A. Budziak, W. Gaśior, *J. Alloys Compd.* **2018**, *732*, 210.
- [67] H. Cheng, H. Jin, H. Liu, N. Cai, C. Gao, P. Zhang, M. Wang, *J. Electroanal. Chem.* **2020**, *878*, 114569.
- [68] G. M. Hobold, C. Wang, K. Steinberg, Y. Li, B. M. Gallant, *Nat. Energy* **2024**, *9*, 580.
- [69] a) Y. Zhang, M. Yao, T. Wang, H. Wu, Y. Zhang, *Angew. Chem., Int. Ed. Engl.* **2024**, *63*, e202403399; b) Y. Liu, X. Tao, Y. Wang, C. Jiang, C. Ma, O. Sheng, G. Lu, X. W. D. Lou, *Science* **2022**, *375*, 739; c) K. Xu, *Chem. Rev.* **2004**, *104*, 4303.

Manuscript received: May 8, 2025

Revised manuscript received: June 11, 2025

Version of record online: